

# Relaxation Dynamics of Enhanced Hot-Electron Flow on Perovskite-Coupled Plasmonic Silver Schottky Nanodiodes

Yujin Park, Jungkweon Choi, Mincheol Kang, Hyunhwa Lee, Hyotcherl Ihee,\* and Jeong Young Park\*

Cite This: *J. Phys. Chem. C* 2021, 125, 2575–2582

Read Online

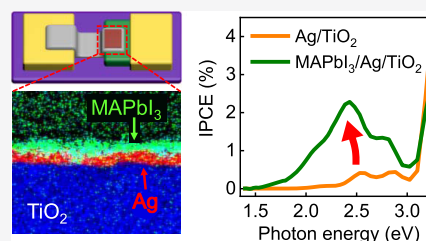
ACCESS |

Metrics & More

Article Recommendations

Supporting Information

**ABSTRACT:** Hot-electron-based photovoltaics has great potential to overcome the limitations of semiconductor-based photovoltaics. However, hot-electron applications still suffer from low quantum efficiency, associated with inefficient hot-electron collection and a poor absorption coefficient. Here, we demonstrate that hot-electron flow on a plasmonic Ag nanodiode is highly enhanced by depositing a MAPbI<sub>3</sub> thin film. Femtosecond transient absorption spectra reveal the hot-electron dynamics, where the hot electrons from MAPbI<sub>3</sub> denote significantly prolonged relaxation time over those from Ag, which can facilitate the internal photoemission process. By comparing the unraveled dynamics of MAPbI<sub>3</sub> on plasmonic Ag to those on a plasmonic Au structure, we found that the former combination exhibits enhanced hot-electron transfer, which is correlated to higher hot-electron flow. We believe that the suggested structure in this work can provide a useful alternative model to design sensitive hot-electron-based photovoltaics.



## INTRODUCTION

With the extensive investigation of strong light–matter interaction on a metal nanostructure, hot-electron dynamics has emerged as a novel pathway for achieving efficient light-harvesting property.<sup>1–3</sup> Noble or coinage metals at nanometer scale, including Au, Ag, Cu, and Al, respond strongly to incident light by generating coherent oscillation of conduction band electrons, called surface plasmon resonance (SPR). The optical excitation of surface plasmons induces strongly localized electric field enhancement near the metal surface, and thus the metal nanostructure can serve as optical antennas.<sup>4–7</sup> The energy of the excited plasmons can be subsequently transferred into individual electrons and holes within a few tens of femtoseconds to generate hot electrons and hot holes, known as Landau damping.<sup>8</sup> Recently, the hot carriers of plasmonic metals have been studied for solar energy conversion due to their attractive advantages compared to conventional semiconductor-based light-harvesting strategies. The collection of the plasmon-driven hot electrons allows us to utilize electrons with energy below the semiconductor band gap. Additionally, it is possible to select a spectrum and polarization mode with a hot-electron-based photodetector.<sup>9–11</sup> In the aspect of photocatalysis, contrary to semiconductors, hot-electron-mediated photocatalysts have super-linear dependence of the chemical reaction rate and quantum efficiency on photon flux and temperature.<sup>12</sup> Despite their outstanding advantages, hot-carrier applications still encounter considerable challenges to achieve high efficiency because of a low absorption coefficient of the plasmonic metal nanostructure and ultrafast relaxation of hot electrons through electron–electron or electron–phonon scattering. Therefore, realizing a sufficient hot-electron population and achieving a slow

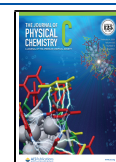
thermalization rate of hot electrons by employing appropriate materials is required to accomplish effective SPR-mediated solar energy conversion. On the basis of the Mie theory, the optical response of plasmonic metals can be determined by considering their real and imaginary parts of the dielectric function.<sup>13</sup>

As the source of surface plasmon, Ag has been known as the best compromise between high absorption and low optical losses, followed by Au, Cu, and Al.<sup>14</sup> In particular, theoretical calculation predicted that Ag exhibits the slowest electron–phonon coupling dynamics and longest maximum carrier lifetime and mean free path among other plasmonic metals.<sup>15</sup> Indeed, Ag shows the greatest near-field enhancement in a visible range<sup>16</sup> and higher hot-electron-driven photocurrent compared to Cu or Au counterparts with comparable thickness.<sup>17,18</sup> To attain further improved SPR-mediated photon conversion efficiency, another approach that integrates plasmonic metals with other light-absorbing materials has been demonstrated.<sup>19–21</sup> Previously, we reported on the enhanced hot-electron flow on plasmonic Au combined with methylammonium lead iodide (MAPbI<sub>3</sub>)<sup>21</sup> due to the increased hot-electron generation from near-field enhancement and the prolonged hot-electron lifetime driven by the inherently slow thermalization rate of the perovskite hot electrons. Since the

Received: January 3, 2021

Revised: January 12, 2021

Published: January 25, 2021



hybrid organic–inorganic perovskites have been reported for their sluggish hot-carrier relaxation dynamics,<sup>22,23</sup> they are in a new class of promising light absorbers for efficient hot-electron-based applications.

In this paper, we describe amplified hot-electron flow on a MAPbI<sub>3</sub>-coupled plasmonic Ag Schottky nanodiode by taking advantage of the strong optical response of Ag and slow hot-electron thermalization dynamics on MAPbI<sub>3</sub>. To reveal the contribution of MAPbI<sub>3</sub> on hot-electron flow, the thickness of a perovskite film was varied by spin-coating different concentrations of perovskite precursor ink. In addition to amplified hot-electron flow, we evaluated the Schottky barrier height, which allows injection of electrons with high energy (hot electrons) and impedes back diffusion of injected carriers by fitting measured current–voltage curves into the thermionic emission model. We also demonstrate different optical excitation modes of SPR on a Ag film by measuring incident photon-to-electron conversion efficiency (IPCE) as a function of photon energy, and show that the SPR peaks are red-shifted due to the MAPbI<sub>3</sub> modification. Lastly, hot-electron relaxation dynamics on Ag and MAPbI<sub>3</sub> were probed using a femtosecond time-resolved transient absorption experiment to explicate the enhancement of hot-electron flow on the MAPbI<sub>3</sub>-modified Ag nanodiode.

## EXPERIMENTAL METHODS

**Fabrication of Perovskite-Modified Silver Schottky Nanodiodes.** To detect hot-electron flow as a steady-state current, a MAPbI<sub>3</sub>-modified silver Schottky nanodiode was fabricated as follows. First, a Ti film (150 nm) was deposited on a thick SiO<sub>2</sub> layer grown on an n-type Si wafer (100), which was aligned with a patterned stainless-steel mask (4 × 7 mm<sup>2</sup>). Then, the Ti film was oxidized at 470 °C for 2 h 10 min to generate a TiO<sub>2</sub> layer (250 nm). To make ohmic electrode pads, Ti (50 nm) and Au (100 nm) layers were deposited consecutively with a second mask (5 × 5 mm<sup>2</sup>) at both ends of the nanodiode. After that, a top Ag thin film (40 nm) was evaporated with a third mask (2 × 6 mm<sup>2</sup>) to generate Ag/TiO<sub>2</sub> Schottky contact. All of the deposition processes were carried out using an e-beam evaporator at <2 × 10<sup>-6</sup> Torr. To change the morphology of a Ag film into a corrugated structure with nanogaps, annealing was conducted under Ar conditions at 300 sccm. To make a MAPbI<sub>3</sub> layer, the perovskite precursor ink, which was prepared using a method described elsewhere,<sup>24</sup> was spin-coated on the top of the nanodiode surface at 4000 rpm for 25 s. During the spin-coating process, toluene was drop-cast to form a dense and uniform surface.<sup>25</sup> Then, the spin-coated film was annealed at 60 °C for 1 min and 100 °C for 9 min to dry the solvent. Last, the fabricated nanodiode was cleaned with a cotton tip soaked with ethanol except for the active area. For a femtosecond time-resolved transient absorption experiment, transparent quartz was used as a substrate to penetrate the pump and probe beam. A TiO<sub>2</sub> layer was formed by annealing the Ti (50 nm) film, and a Ag thin film (20 nm) was deposited on the TiO<sub>2</sub> layer. For a MAPbI<sub>3</sub> layer, perovskite precursor ink with a concentration of 150 mM was used to absorb sufficient photons.

**Characterization and Measurement.** The cross-sectional morphology and elemental distribution of the nanodiode were characterized by transmission electron microscopy (TEM, Talos F200X) equipped with an energy-dispersive X-ray spectroscopy (EDS) system. The thin TEM specimen was prepared by a focused ion beam (FIB, FEI Helios Nanolab 450

F1) milling process with a carbon protection layer. A source meter (Keithley instrument 2400) was used to measure the current–voltage characteristics and short-circuit photocurrents. For the incident light source, a broad visible light emitted from a tungsten–halogen lamp with an intensity of 9 mW/cm<sup>2</sup> was employed. The incident photon-to-current conversion efficiency (IPCE) was measured with a tunable light source that provided a wavelength from 380 to 900 nm (Newport, TLS-300XU). The morphology of the Ag thin layer was analyzed with a scanning electron microscopy (SEM, Hitachi SU5000) and a commercial atomic force microscopy system (AFM, Agilent 5500). For the AFM characterization, Pt/Ir-coated silicon cantilevers (Nanosensors, PPP-CONTPT-50) were used with a spring constant of 0.2 N/m. The absorption spectrum for TiO<sub>2</sub> and Ag/TiO<sub>2</sub> was measured with a UV–vis spectrophotometer (Hitachi, UV 3600). To obtain femtosecond time-resolved absorption spectra, a pump–probe transient absorption spectroscopy system was employed, which utilized seed pulses generated from a Ti:Sapphire laser (Spectra Physics, MaiTai SP). The output pulses with the wavelength of 800 nm were generated by a regenerative amplifier Ti:Sapphire laser system (Spectra Physics, Spitfire Ace, 1 kHz), which was pumped by a diode-pumped Q-switched laser (Spectra Physics, Empower). An optical parametric amplifier (Spectra Physics, TOPAS prime) was used to provide the excitation beam of 420 nm (2.95 eV). A part of the fundamental beam (800 nm) was focused to generate a white light continuum as a probe beam. The probe pulse was transmitted and was detected by a CCD detector attached to an absorption spectroscope. The pump pulse was chopped by a mechanical chopper synchronized to one-half of the laser repetition rate, resulting in a pair of spectra with and without the pump, from which the absorption change induced by the pump pulse was estimated.

## RESULTS AND DISCUSSION

Figure 1a illustrates a scheme of the MAPbI<sub>3</sub>-modified Ag Schottky nanodiode. The Schottky contact region, which is composed of MAPbI<sub>3</sub>, Ag, and TiO<sub>2</sub> layers with an area of 4 × 4 mm<sup>2</sup>, is located in the middle of the nanodiode. The principle of detecting hot-electron flow is described in Figure 1b. Since Ag has a greater Fermi level compared to MAPbI<sub>3</sub> and TiO<sub>2</sub>, two Schottky barriers are formed at both MAPbI<sub>3</sub>/Ag and Ag/TiO<sub>2</sub> interfaces. Upon irradiation, the MAPbI<sub>3</sub> film and the Ag layer absorb photons to generate hot electrons, which have high kinetic energies. The excited hot electrons, which are available to overcome energy barriers, including the built-in potential ( $eV_{bi}$ ) within MAPbI<sub>3</sub> and the Schottky barrier height ( $E_{SB}$ ), are injected into the TiO<sub>2</sub> layer and produce a steady-state current. Considering the mean free path of hot electrons (16–600 nm),<sup>23,26</sup> the thickness of the MAPbI<sub>3</sub> film has to be within a few tens of nanometers. Thus, we changed the thicknesses using different concentrations of perovskite precursor ink from 40 to 90 mM, and the thicknesses were measured in the range of 30–51 nm (Figure S1). To characterize the morphology and elemental distribution of the active area, a qualitative investigation was carried out by taking high-angle annular dark-field (HAADF) and scanning transmission electron microscopy (STEM) images, as shown in Figure 1c. In addition, the elemental mapping image characterized by energy-dispersive X-ray spectroscopy (EDS) is shown in Figure 1d. The distinctive elemental distribution of the corresponding image is represented in Figure S2. These

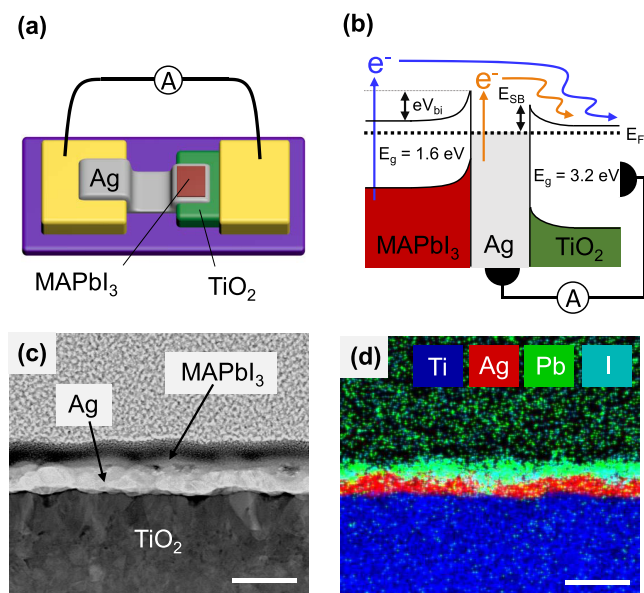


**Figure 1.** (a) Schematic illustration of a MAPbI<sub>3</sub> thin film modified with a plasmonic Ag Schottky nanodiode. (b) Principle for detecting hot-electron flow on the MAPbI<sub>3</sub>-modified plasmonic Ag nanodiode. Hot electrons that are excited on the MAPbI<sub>3</sub> film with a Ag layer have high kinetic energy to overcome both the built-in potential ( $eV_{bi}$ ) and the Schottky barrier ( $E_{SB}$ ), and can be injected into the TiO<sub>2</sub> to generate steady-state current. (c) Cross-sectional high-angle annular dark-field (HAADF) and scanning transmission electron microscopy (STEM) images. (d) The corresponding elemental energy-dispersive X-ray spectroscopy (EDS) mapping image for the MAPbI<sub>3</sub>/Ag/TiO<sub>2</sub> structure. Scale bars in the images are 100 nm.

data confirm that the Ag thin layer was uniformly deposited on the TiO<sub>2</sub> layer, and the Ag film was fully covered by the MAPbI<sub>3</sub> thin film, as we intended.

To verify the formation of the Schottky barrier, current–voltage ( $I$ – $V$ ) characteristics were measured by applying bias from  $-1$  to  $1$  V across the two electrode pads (Figure S3), and the Schottky barrier heights of nanodiodes were obtained by fitting  $I$ – $V$  curves with the thermionic emission model (Table S1). According to the results, all of the fabricated nanodiodes exhibit the rectifying behavior regardless of perovskite film modification, and the Schottky barrier heights show little change with perovskite modification.

To estimate hot-electron-mediated photoelectrical performance, we measured short-circuit photocurrent on the fabricated nanodiodes, as shown in Figure 2a. Prior to perovskite film deposition, the pristine Ag nanodiode shows a photocurrent of 39 nA, but it is further increased to 175, 225, and 370 nA on the Ag nanodiodes modified with 40, 60, and 80 mM MAPbI<sub>3</sub> precursor ink, respectively. This is because hot electrons are generated from not only the Ag layer but also the MAPbI<sub>3</sub> thin film, which serves as a photosensitizer to provide hot electrons. Furthermore, a thicker MAPbI<sub>3</sub> layer helps absorb more incident photons and thus naturally contributes to the increase in photocurrent. However, when the thickness of the MAPbI<sub>3</sub> film reaches 51 nm (90 mM MAPbI<sub>3</sub> precursor ink), the photocurrent decreases to 205 nA.

There are two competing processes for a thick MAPbI<sub>3</sub> layer: one is to improve hot-electron generation due to efficient light absorption in MAPbI<sub>3</sub>, and the other is to decrease the hot-electron flow caused by a low probability of hot-electron transfer due to their inelastic scattering within their mean free

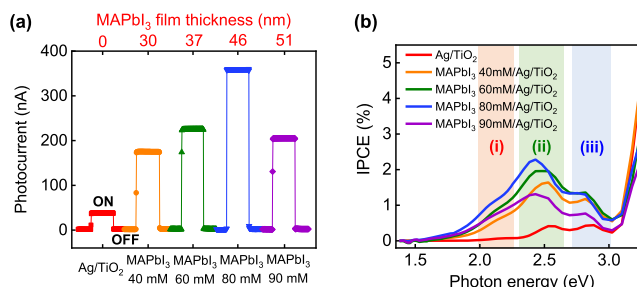


**Figure 2.** (a) Measured short-circuit photocurrents and (b) incident photon-to-electron conversion efficiency (IPCE) results as a function of photon energy on the MAPbI<sub>3</sub>-modified Ag nanodiodes according to different thicknesses of MAPbI<sub>3</sub> thin films. The pristine Ag layer with a rough surface supported on the TiO<sub>2</sub> layer indicates three surface plasmon resonance (SPR) peaks at 2.17, 2.55, and 2.84 eV at the photon energy regions (i), (ii), and (iii), respectively.

paths and diminished photon absorption of the Ag film. In this case, 51 nm of MAPbI<sub>3</sub> film modification leads to a decrease in hot-electron flow because the total sum of MAPbI<sub>3</sub> and Ag film thickness exceeds the mean free path of hot electrons and the unfavorable  $E$ -field enhancement effect and hot-electron generation on the Ag film due to decreased light absorption. In addition to the short-circuit photocurrent measurement, IPCE as a function of photon energy was also probed, as shown in Figure 2b. The IPCE can be described as the following equation

$$\text{IPCE} = \frac{hc}{e\lambda} \left[ \frac{J_{SC} \text{ (nA/cm}^2\text{)}}{P_{in} \text{ (nW/cm}^2\text{)}} \right] \times 100\% \quad (1)$$

where  $h$  is the Planck constant,  $c$  is the speed of light,  $J_{SC}$  is the short-circuit photocurrent density,  $P_{in}$  is the power of incident light,  $e$  is the elementary charge, and  $\lambda$  is the wavelength. According to the IPCE results, the MAPbI<sub>3</sub>-modified Ag nanodiodes show higher photon conversion efficiency than the pristine Ag nanodiode over the entire visible light range. Besides, the deposition of 51 nm of the MAPbI<sub>3</sub> film leads to a decrease in IPCE compared to the nanodiodes modified with thinner perovskite films, which follows the trend set by the short-circuit photocurrent results. Therefore, the results support that the measured photocurrent mainly originates from hot electrons, and it can be increased with modification of a thicker perovskite film, so long as the thickness of the perovskite film does not exceed the mean free path of hot electrons.

Detailed inspection of the IPCE results shows that the pristine Ag nanodiode has three distinct peaks in the visible light range and a sudden increase over 3.2 eV. The rapid IPCE increase over 3.2 eV is attributed to interband excitation in the TiO<sub>2</sub> layer. When it comes to the three peaks, they are located at 2.17, 2.55, and 2.84 eV at the photon energy regions (i), (ii), and (iii), respectively, which correspond to localized SPR peaks of a Ag nanostructure.<sup>17,27,28</sup> It has been reported that the SPR peaks of Ag are very sensitive to inherent geometry and morphology.<sup>29–31</sup> For example, spherical silver nanoparticles exhibit a single polarization mode at 400 nm, which corresponds to dipolar charge distribution. Meanwhile, as the asymmetry of the nanoparticles becomes greater from cuboctahedron to cube, the nanoparticles reveal a high order of multipole resonance with a red shift of the resonance peaks.<sup>32</sup> This is because asymmetric geometry responds

nonuniformly to the incident electromagnetic field, which leads to phase retardation of the  $E$ -field within the structure and apparent high order polarization modes including quadrupole, octupole, hexadecapole, etc.<sup>31</sup> The morphology of the pristine Ag nanodiode was characterized using atomic force microscopy (AFM), which exhibits a thickness of 40 nm and a root-mean-square (RMS) roughness of 5.2 nm (Figure S4a). Moreover, we confirmed that convex surfaces of 40 nm thick Ag film have an arbitrary shape with an AFM topography image (Figure S4b). Therefore, it is plausible that the three distinguishable peaks are observed in the visible light spectrum on the fabricated pristine Ag nanodiode. To further clarify the origin of three peaks, we measured IPCE on pristine Ag nanodiodes with a 25 nm thick Ag film and an annealed 25 nm thick Ag film (Figure S5a). As shown in the SEM images (Figure S5b,c), the morphology of the Ag layer was changed into a corrugated surface, creating nanometer-sized gaps between Ag clusters with heat treatment at 110 °C for 30 min. Accordingly, the SPR peaks of Ag become noticeable with a thinner and bumpier surface. Therefore, we can assign the three peaks to the different SPR modes of the Ag layer.

Notably, these three individual peaks tend to be red-shifted with MAPbI<sub>3</sub> film modification. The variation of the peak position with the deposition of different thicknesses of MAPbI<sub>3</sub> is shown in Figure 3a, and IPCE values for each of the peaks

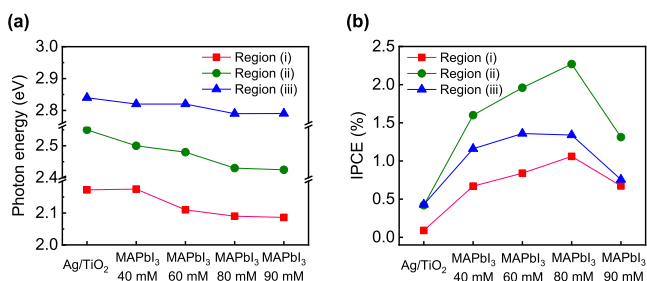


**Figure 3.** (a) Variations of the Ag SPR peak position and (b) IPCE values for the peaks with respect to the modification of different MAPbI<sub>3</sub> thicknesses at the photon energy regions (i), (ii), and (iii). Individual Ag SPR peaks tend to be red-shifted with MAPbI<sub>3</sub> film modification, and the IPCE values of the SPR peaks are increased with thicker perovskite film modification, unless the total sum of Ag and MAPbI<sub>3</sub> thickness exceeds the hot-electron mean free path.

are represented in Figure 3b. Generally, the position of the SPR peak is influenced by the refractive index ( $n$ ) of the physical environment.<sup>33,34</sup> This is because the opposite direction of the medium-induced field to that of plasmonic metal polarization results in attenuation of oscillation frequency. Therefore, the metal nanostructures surrounded by a higher refractive index show a red-shifted SPR wavelength despite the same geometry.<sup>32</sup> The earlier reports have found that  $n$  of MAPbI<sub>3</sub> ( $n = 2.3$ )<sup>35–37</sup> is higher than that of air ( $n = 1$ ) in the visible range. Furthermore, the thick and compact MAPbI<sub>3</sub> film may allow small number of voids, leading to a higher  $n$ .<sup>38</sup> Therefore, the red-shifted resonance peaks of Ag with perovskite film deposition can be explained by the increasing refractive index of the surrounding medium. According to the previous literature,<sup>21</sup> the variation of the localized surface plasmon resonance (LSPR) peak position of Au is negligible with MAPbI<sub>3</sub> modification. Since the LSPR wavelength is determined by achieving the Fröhlich condition ( $\epsilon_r = -2\epsilon_m$ , where  $\epsilon_r$  is the real part of the metal dielectric

function and  $\epsilon_m$  is the relative dielectric constant of the medium), the higher refractive index sensitivity for Ag is attributed to its greater change in the real part dielectric constant than that of Au.<sup>39</sup> In addition, the photocurrent dependence of the red-shifted SPR peaks on MAPbI<sub>3</sub> film thickness persists as long as ballistic hot-electron transport can be achieved. Therefore, the observation of red-shifted plasmonic modes with MAPbI<sub>3</sub> modification signifies that strong coupling between Ag and MAPbI<sub>3</sub> is formed that can drive improved optical response and hot-electron flow.

Such strong light–matter interaction on MAPbI<sub>3</sub>-modified Ag can be further improved by changing the morphology of Ag. Owing to the high extinction cross section of Ag, even a Ag thin-film structure with the rough surface has a strong SPR effect. However, when we changed the morphology of the Ag film into a corrugated surface with nanometer-sized gaps by modest heat treatment at 95 °C for 15 min, a further enhanced SPR effect was achieved. This can be supported by enhanced photocurrent on an annealed Ag thin film, as shown in Figure 4. When we modify both neat Ag film and annealed Ag film

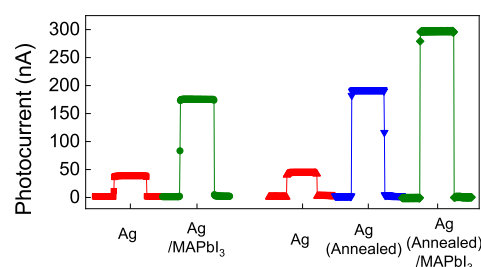


**Figure 4.** Short-circuit photocurrent measured on an identical concentration of MAPbI<sub>3</sub> precursor ink (40 mM)-modified Ag nanodiodes with different morphologies of the Ag layer.

with the same concentration of MAPbI<sub>3</sub> precursor ink, we can observe photocurrent enhancement on both structures. However, a MAPbI<sub>3</sub>-modified annealed Ag film structure exhibits a much higher photocurrent of 297 nA, while its MAPbI<sub>3</sub>-modified neat Ag counterpart shows a lower value of 175 nA. This is associated with greater hot-electron flow on the MAPbI<sub>3</sub> and annealed Ag layers due to a stronger SPR intensity.

To understand the hot-electron relaxation dynamics on a perovskite-modified Ag Schottky nanodiode, we carried out a femtosecond time-resolved transient absorption (TA) experiment for a MAPbI<sub>3</sub>/Ag/TiO<sub>2</sub> structure. The sample preparation procedure for the TA experiment was modified from the Schottky nanodiode fabrication process to acquire proper signals, which is described in the Supporting Information. The TA spectra recorded on a MAPbI<sub>3</sub>/Ag/TiO<sub>2</sub> structure excited at 2.95 eV with early delay times ( $\sim 9.5$  ps) and late delay times ( $\sim 198$  ps) are shown in Figure 5a,b, respectively. According to the obtained TA spectra, we can notice typical features of MAPbI<sub>3</sub>, including two negative photobleaching peaks at 1.7 and 2.45 eV, which coincide with state-filling at the band edge and subband gap states,<sup>40</sup> respectively. Besides, broad photoinduced absorption appears between two negative valleys, which corresponds to refractive index changes caused by photoexcited states in MAPbI<sub>3</sub>.<sup>41</sup> Meanwhile, we also discern an additional negative band at 2.65 eV for the MAPbI<sub>3</sub>/Ag/TiO<sub>2</sub> structure, which disappears in longer delay times while the signals from MAPbI<sub>3</sub> are still well preserved. This result implies that the decay time of the origin

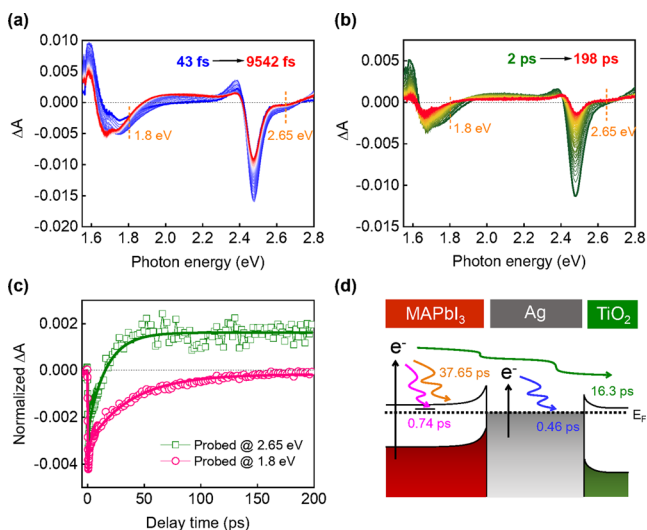


**Figure 5.** Transient absorption spectra for a MAPbI<sub>3</sub>/Ag/TiO<sub>2</sub> structure recorded at (a) early delay times (43 fs to 9.5 ps) and (b) late delay times (2–198 ps) pumped at a photon energy of 2.95 eV. (c) Hot-electron relaxation dynamics probed at 2.65 eV for Ag and 1.8 eV for MAPbI<sub>3</sub>. The solid line curves represent fitted results. (d) Schematic illustration of hot-electron relaxation and extraction on the MAPbI<sub>3</sub>/Ag/TiO<sub>2</sub> structure.

of the negative bleaching peak at 2.65 eV is much faster than that of the excited electron in MAPbI<sub>3</sub>. To elucidate the origin of the photobleaching peak at 2.65 eV, we measured the steady-state absorption spectrum for TiO<sub>2</sub> and Ag/TiO<sub>2</sub> structures (Figure S6). As shown in Figure S6, Ag/TiO<sub>2</sub> indicates a strong absorption peak at 2.65 eV that is not observed in bare TiO<sub>2</sub>, indicating that the peak can be assigned to an SPR peak of Ag. Therefore, the negative band centered at 2.65 eV of the TA spectra results from surface plasmon-induced hot electrons on Ag.

To estimate the relaxation time of hot electrons from Ag and MAPbI<sub>3</sub>, the time profiles monitored at 2.65 and 1.8 eV fit a biexponential function, as shown in Figure 5c. Since the high-energy tail showing exponential decay ranging from 1.7 to 2.1 eV originated from redistribution of nonequilibrium hot electrons on MAPbI<sub>3</sub>, whose temperature can be determined using the Maxwell–Boltzmann equation,<sup>22</sup> dynamics probed at 1.8 eV were traced to obtain the MAPbI<sub>3</sub> hot-electron relaxation time. The acquired time constants are summarized in Table 1. The decay profile probed at 1.8 eV represents two

**Table 1.** List of Acquired Time Constants for the MAPbI<sub>3</sub>/Ag/TiO<sub>2</sub> Structure

	$\tau_1$ (ps)	$\tau_2$ (ps)
probed@1.8 eV	$0.74 \pm 0.09$	$37.65 \pm 0.98$
probed@2.65 eV	$0.46 \pm 0.05$	$16.3 \pm 0.78$

time constants, where the fast time component (0.75 ps) is commensurate with hot-electron quenching through trap states,<sup>21</sup> and the long time component (37.65 ps) indicates time comparable to the hot-electron thermalization rate within the MAPbI<sub>3</sub> conduction band.<sup>22,23</sup> For the probe photon energy of 2.65 eV, 0.46 and 16.3 ps are determined. As the amplitude of the negative bleaching peak at 2.65 eV rapidly decreases and subsequently produces rising features, we can infer that rapid hot-electron relaxation occurs early on (0.46

ps), but some portion of electrons are still at excited states. Therefore, we suggest that the 0.46 ps results from hot-electron thermalization within the Ag layer,<sup>42,43</sup> and 16.3 ps probably originated from the injection rate of MAPbI<sub>3</sub> hot electrons into the TiO<sub>2</sub> acceptor layer, as shown in Figure 5d. The hot-electron injection rate of perovskite<sup>23</sup> or plasmonic metal<sup>44</sup> into the adjacent acceptor layer is reported at a sub-picosecond timescale, which is within the resolution of our setup. However, the hot carriers from perovskite in our system have to pass through the Ag layer to reach TiO<sub>2</sub> so that the injection rate could be delayed by electron scattering due to a large discordance of electron effective mass. In addition, the acquired injection rate, indicated within the range of hot-electron lifetime of MAPbI<sub>3</sub> but longer than that of Ag, supports our assumption. Markedly, hot-electron relaxation time of MAPbI<sub>3</sub> is much longer than that of Ag, indicating that the probability of hot-electron transfer into an electron acceptor layer (TiO<sub>2</sub>) is highly improved on MAPbI<sub>3</sub>-modified Ag nanodiodes compared to their pristine Ag counterparts. In addition, the presence of injected hot-electron lifetime of MAPbI<sub>3</sub> (16.3 ps) assists successful internal photoemission of surface plasmon-induced hot electrons.

As stated in the previous literature,<sup>21</sup> the pristine 15 nm thick Au film nanodiode showed a photocurrent of 25 nA, while the pristine 40 nm thick Ag film nanodiode in this work indicates 39 nA. Despite the higher probability of hot-electron inelastic scattering on the Ag film due to its greater thickness, the Ag nanodiode represents higher response to the light to produce hot-electron flow. This can be attributed to the inherent excellent plasmonic property of Ag, including its very high optical extinction and strong field enhancement.<sup>16,45</sup> When the same perovskite precursor ink of 80 mM with a single layer is deposited on both Au and Ag nanodiodes, the photocurrent of the MAPbI<sub>3</sub>-modified Au nanodiode results in 35 nA, while that of the MAPbI<sub>3</sub>-modified Ag nanodiode exhibits 360 nA, which is 10.3 times higher than the photocurrent measured on the MAPbI<sub>3</sub>-modified Au structure. We attribute such higher hot-electron flow on the MAPbI<sub>3</sub>-coupled Ag structure to enhanced hot-electron generation due to stronger near-field enhancement of Ag and facilitated hot-electron transfer to the acceptor layers (Ag and TiO<sub>2</sub>). Compared to a MAPbI<sub>3</sub>-modified Au structure, a MAPbI<sub>3</sub>-coupled Ag structure shows a weaker initial TA signal at the MAPbI<sub>3</sub> hot-electron bleaching band ( $\lambda_{\text{probe}} = 1.8$  eV), which is  $-0.004$  for MAPbI<sub>3</sub>/Ag and  $-0.009$  for MAPbI<sub>3</sub>/Au structures even though the same thickness of the MAPbI<sub>3</sub> layer was deposited. Moreover, we observed a shortened hot-electron lifetime of MAPbI<sub>3</sub>, which is 37.65 ps for MAPbI<sub>3</sub>/Ag and 67.38 ps for MAPbI<sub>3</sub>/Au. Since the intensity of the TA signal is related to the carrier temperature based on the Maxwell–Boltzmann equation, the weaker TA signal on the MAPbI<sub>3</sub>-coupled Ag structure can be interpreted as hot electrons, with high energies transferred into the acceptor layers.<sup>23</sup> Correspondingly, the quenched hot-electron lifetime obtained on the MAPbI<sub>3</sub>/Ag structure implies an enhanced hot-electron transfer process.<sup>46,47</sup> Therefore, the comparison results signify that the combined structure of perovskite and plasmonic metals is beneficial to boosting hot-electron flow, and Ag exhibits a stronger coupling effect with MAPbI<sub>3</sub> in a more significant way than Au by showing greater near-field enhancement due to higher SPR intensity and improved hot-electron transfer. Here, we choose a thicker Ag film (40 nm) than the Au film (15 nm), which was used in an earlier study<sup>21</sup>

because the higher surface energy of the 15 nm thick Ag layer leads to an electrically disconnected circuit during MAPbI<sub>3</sub> layer deposition. Hence, the field is open for research to optimize the thicknesses of layers to achieve both maximized hot-electron flow and stable devices. As this is in its initial stage, there is room for advancement on the quantum efficiency of a MAPbI<sub>3</sub>-modified Ag structure. To maximize photoconversion efficiency, further investigation is needed into optimizing layer thicknesses or adopting a silver nanostructure such as nanorods,<sup>10</sup> nanostripes,<sup>48</sup> or a grating system.<sup>49</sup>

## CONCLUSIONS

In summary, we have demonstrated the enhanced hot-electron flow on MAPbI<sub>3</sub>-coupled plasmonic Ag Schottky nanodiodes. The photon conversion efficiency of the plasmonic Ag nanodiodes modified with different thicknesses of the MAPbI<sub>3</sub> layer was analyzed by measuring short-circuit photocurrent and IPCE as a function of incident photon energy. The enhancement of hot-electron flow with MAPbI<sub>3</sub> modification can be ascribed to additional hot-electron flow generated from MAPbI<sub>3</sub> and a slow relaxation rate of MAPbI<sub>3</sub> hot electrons, which contributes to increasing the probability of hot-electron injection. However, MAPbI<sub>3</sub> coupled with plasmonic Ag exhibits even greater hot-electron flux enhancement compared to the MAPbI<sub>3</sub>-modified plasmonic Au structure due to stronger optical response of plasmonic Ag and effective hot-electron transfer identified by an ultrafast pump–probe experiment. Indeed, we acquired a hot-electron injection rate of 16.3 ps on MAPbI<sub>3</sub>-coupled Ag structures, which indicates the presence of separated hot electrons. Moreover, we observed three distinguishable SPR peaks of the Ag layer generated by its asymmetric geometry. They are red-shifted with MAPbI<sub>3</sub> modification due to changes in the environmental dielectric, which supports strong coupling between plasmonic Ag and MAPbI<sub>3</sub> layers. We believe our findings offer a high potential of MAPbI<sub>3</sub> coupled with the plasmonic Ag structure for achieving efficient light-harvesting property and provide an alternative guideline for designing sensitive hot-electron-based photovoltaics.

## ASSOCIATED CONTENT

### Supporting Information

The Supporting Information is available free of charge at <https://pubs.acs.org/doi/10.1021/acs.jpcc.1c00033>.

The detailed information on thicknesses of the MAPbI<sub>3</sub> thin films, EDS elemental mapping images, *I*–*V* curves, the characterization of the Ag layer morphology, TA spectra, and the absorption of samples (PDF)

## AUTHOR INFORMATION

### Corresponding Authors

**Hyocheol Ihee** – Department of Chemistry and KI for the BioCentury, Korea Advanced Institute of Science and Technology (KAIST), Daejeon 34141, Republic of Korea; Center for Nanomaterials and Chemical Reactions, Institute for Basic Science (IBS), Daejeon 34141, Republic of Korea; [orcid.org/0000-0003-0397-5965](https://orcid.org/0000-0003-0397-5965); Email: [hyotcherl.ihee@kaist.ac.kr](mailto:hyotcherl.ihee@kaist.ac.kr)

**Jeong Young Park** – Department of Chemistry, Korea Advanced Institute of Science and Technology (KAIST), Daejeon 34141, Republic of Korea; Center for Nanomaterials and Chemical Reactions, Institute for Basic Science (IBS),

Daejeon 34141, Republic of Korea; [orcid.org/0000-0002-8132-3076](https://orcid.org/0000-0002-8132-3076); Email: [jeongypark@kaist.ac.kr](mailto:jeongypark@kaist.ac.kr)

## Authors

**Yujin Park** – Department of Chemistry, Korea Advanced Institute of Science and Technology (KAIST), Daejeon 34141, Republic of Korea; Center for Nanomaterials and Chemical Reactions, Institute for Basic Science (IBS), Daejeon 34141, Republic of Korea

**Jungkweon Choi** – Department of Chemistry and KI for the BioCentury, Korea Advanced Institute of Science and Technology (KAIST), Daejeon 34141, Republic of Korea; Center for Nanomaterials and Chemical Reactions, Institute for Basic Science (IBS), Daejeon 34141, Republic of Korea

**Mincheol Kang** – Department of Chemistry, Korea Advanced Institute of Science and Technology (KAIST), Daejeon 34141, Republic of Korea; Center for Nanomaterials and Chemical Reactions, Institute for Basic Science (IBS), Daejeon 34141, Republic of Korea

**Hyunhwa Lee** – Department of Chemistry, Korea Advanced Institute of Science and Technology (KAIST), Daejeon 34141, Republic of Korea; Center for Nanomaterials and Chemical Reactions, Institute for Basic Science (IBS), Daejeon 34141, Republic of Korea

Complete contact information is available at:

<https://pubs.acs.org/10.1021/acs.jpcc.1c00033>

## Author Contributions

Y.P. and J.C. contributed equally to this work. This manuscript was written through the contributions of all authors. All authors have given approval to the final version of the manuscript.

## Notes

The authors declare no competing financial interest.

## ACKNOWLEDGMENTS

This work was supported by the Institute for Basic Science (IBS-R004).

## REFERENCES

- (1) Brongersma, M. L.; Halas, N. J.; Nordlander, P. Plasmon-Induced Hot Carrier Science and Technology. *Nat. Nanotechnol.* **2015**, *10*, 25–34.
- (2) Clavero, C. Plasmon-Induced Hot-Electron Generation at Nanoparticle/Metal-Oxide Interfaces for Photovoltaic and Photocatalytic Devices. *Nat. Photonics* **2014**, *8*, 95–103.
- (3) Amendola, V.; Pilot, R.; Frascioni, M.; Marago, O. M.; Iati, M. A. Surface Plasmon Resonance in Gold Nanoparticles: A Review. *J. Phys.: Condens. Matter* **2017**, *29*, No. 203002.
- (4) Guo, C. F.; Sun, T. Y.; Cao, F.; Liu, Q.; Ren, Z. F. Metallic Nanostructures for Light Trapping in Energy-Harvesting Devices. *Light: Sci. Appl.* **2014**, *3*, No. e161.
- (5) Atwater, H. A.; Polman, A. Plasmonics for Improved Photovoltaic Devices. *Nat. Mater.* **2010**, *9*, 205–213.
- (6) Lee, H.; Lee, H.; Park, J. Y. Direct Imaging of Surface Plasmon-Driven Hot Electron Flux on the Au Nanoprism/TiO<sub>2</sub>. *Nano Lett.* **2019**, *19*, 891–896.
- (7) Zhang, C.; Zhao, H. Q.; Zhou, L. A.; Schlather, A. E.; Dong, L. L.; McClain, M. J.; Swearer, D. F.; Nordlander, P.; Halas, N. J. Al-Pd Nanodisk Heterodimers as Antenna-Reactor Photocatalysts. *Nano Lett.* **2016**, *16*, 6677–6682.
- (8) Lee, Y. K.; Lee, H.; Lee, C.; Hwang, E.; Park, J. Y. Hot-Electron-Based Solar Energy Conversion with Metal-Semiconductor Nanodiodes. *J. Phys.: Condens. Matter* **2016**, *28*, No. 254006.

- (9) Lee, C.; Lee, Y. K.; Park, Y.; Park, J. Y. Polarization Effect of Hot Electrons in Tandem-Structured Plasmonic Nanodiode. *ACS Photonics* **2018**, *5*, 3499–3506.
- (10) Knight, M. W.; Sobhani, H.; Nordlander, P.; Halas, N. J. Photodetection with Active Optical Antennas. *Science* **2011**, *332*, 702–704.
- (11) Sarkar, S.; Gupta, V.; Kumar, M.; Schubert, J.; Probst, P. T.; Joseph, J.; Konig, T. A. F. Hybridized Guided-Mode Resonances via Colloidal Plasmonic Self-Assembled Grating. *ACS Appl. Mater. Interfaces* **2019**, *11*, 13752–13760.
- (12) Christopher, P.; Xin, H. L.; Marimuthu, A.; Linic, S. Singular Characteristics and Unique Chemical Bond Activation Mechanisms of Photocatalytic Reactions on Plasmonic Nanostructures. *Nat. Mater.* **2012**, *11*, 1044–1050.
- (13) Rycenga, M.; Cobley, C. M.; Zeng, J.; Li, W. Y.; Moran, C. H.; Zhang, Q.; Qin, D.; Xia, Y. N. Controlling the Synthesis and Assembly of Silver Nanostructures for Plasmonic Applications. *Chem. Rev.* **2011**, *111*, 3669–3712.
- (14) Mascaretti, L.; Dutta, A.; Kment, S.; Shalaev, V. M.; Boltasseva, A.; Zboril, R.; Naldoni, A. Plasmon-Enhanced Photoelectrochemical Water Splitting for Efficient Renewable Energy Storage. *Adv. Mater.* **2019**, *31*, No. 1805513.
- (15) Brown, A. M.; Sundararaman, R.; Narang, P.; Goddard, W. A.; Atwater, H. A. Nonradiative Plasmon Decay and Hot Carrier Dynamics: Effects of Phonons, Surfaces, and Geometry. *ACS Nano* **2016**, *10*, 957–966.
- (16) Tanabe, K. Field Enhancement around Metal Nanoparticles and Nanoshells: A Systematic Investigation. *J. Phys. Chem. C* **2008**, *112*, 15721–15728.
- (17) Lee, H.; Lee, Y. K.; Hwang, E.; Park, J. Y. Enhanced Surface Plasmon Effect of Ag/TiO<sub>2</sub> Nanodiodes on Internal Photoemission. *J. Phys. Chem. C* **2014**, *118*, 5650–5656.
- (18) Lee, C.; Park, Y.; Park, J. Y. Hot Electrons Generated by Intraband and Interband Transition Detected Using a Plasmonic Cu/TiO<sub>2</sub> Nanodiode. *RSC Adv.* **2019**, *9*, 18371–18376.
- (19) McFarland, E. W.; Tang, J. A Photovoltaic Device Structure Based on Internal Electron Emission. *Nature* **2003**, *421*, 616–618.
- (20) Lee, Y. K.; Park, J.; Park, J. Y. The Effect of Dye Molecules and Surface Plasmons in Photon-Induced Hot Electron Flows Detected on Au/TiO<sub>2</sub> Nanodiodes. *J. Phys. Chem. C* **2012**, *116*, 18591–18596.
- (21) Park, Y.; Choi, J.; Lee, C.; Cho, A. N.; Cho, D. W.; Park, N. G.; Ihee, H.; Park, J. Y. Elongated Lifetime and Enhanced Flux of Hot Electrons on a Perovskite Plasmonic Nanodiode. *Nano Lett.* **2019**, *19*, 5489–5495.
- (22) Yang, Y.; Ostrowski, D. P.; France, R. M.; Zhu, K.; van de Lagemaat, J.; Luther, J. M.; Beard, M. C. Observation of a Hot-Phonon Bottleneck in Lead-Iodide Perovskites. *Nat. Photonics* **2016**, *10*, 53–59.
- (23) Li, M. J.; Bhaumik, S.; Goh, T. W.; Kumar, M. S.; Yantara, N.; Gratzel, M.; Mhaisalkar, S.; Mathews, N.; Sum, T. C. Slow Cooling and Highly Efficient Extraction of Hot Carriers in Colloidal Perovskite Nanocrystals. *Nat. Commun.* **2017**, *8*, No. 14350.
- (24) Ahn, N.; Son, D. Y.; Jang, I. H.; Kang, S. M.; Choi, M.; Park, N. G. Highly Reproducible Perovskite Solar Cells with Average Efficiency of 18.3% and Best Efficiency of 19.7% Fabricated via Lewis Base Adduct of Lead(II) Iodide. *J. Am. Chem. Soc.* **2015**, *137*, 8696–8699.
- (25) Jeon, N. J.; Noh, J. H.; Kim, Y. C.; Yang, W. S.; Ryu, S.; Seok, S. I. Solvent Engineering for High-Performance Inorganic–Organic Hybrid Perovskite Solar Cells. *Nat. Mater.* **2014**, *13*, 897–903.
- (26) Guo, Z.; Wan, Y.; Yang, M. J.; Snaider, J.; Zhu, K.; Huang, L. B. Long-Range Hot-Carrier Transport in Hybrid Perovskites Visualized by Ultrafast Microscopy. *Science* **2017**, *356*, 59–62.
- (27) Lazzari, R.; Roux, S.; Simonsen, I.; Jupille, J.; Bedeaux, D.; Vlioger, J. Multipolar Plasmon Resonances in Supported Silver Particles: The Case of Ag/Alpha-Al<sub>2</sub>O<sub>3</sub>(0001). *Phys. Rev. B* **2002**, *65*, No. 235424.
- (28) Gao, X. D.; Fei, G. T.; Xu, S. H.; Zhong, B. N.; Ouyang, H. M.; Li, X. H.; Zhang, L. D. Porous Ag/TiO<sub>2</sub>-Schottky-Diode Based Plasmonic Hot-Electron Photodetector with High Detectivity and Fast Response. *Nanophotonics* **2019**, *8*, 1247–1254.
- (29) Hooshmand, N.; El-Sayed, M. A. Collective Multipole Oscillations Direct the Plasmonic Coupling at the Nanojunction Interfaces. *Proc. Natl. Acad. Sci. U.S.A.* **2019**, *116*, 19299–19304.
- (30) Sosa, I. O.; Noguez, C.; Barrera, R. G. Optical Properties of Metal Nanoparticles with Arbitrary Shapes. *J. Phys. Chem. B* **2003**, *107*, 6269–6275.
- (31) Yin, J.; Zang, Y. S.; Xu, B. B.; Li, S. P.; Kang, J. Y.; Fang, Y. Y.; Wu, Z. H.; Li, J. Multipole Plasmon Resonances in Self-Assembled Metal Hollow-Nanospheres. *Nanoscale* **2014**, *6*, 3934–3940.
- (32) Noguez, C. Surface Plasmons on Metal Nanoparticles: The Influence of Shape and Physical Environment. *J. Phys. Chem. C* **2007**, *111*, 3806–3819.
- (33) Xu, G.; Tazawa, M.; Jin, P.; Nakao, S. Surface Plasmon Resonance of Sputtered Ag Films: Substrate and Mass Thickness Dependence. *Appl. Phys. A* **2005**, *80*, 1535–1540.
- (34) Kelly, K. L.; Coronado, E.; Zhao, L. L.; Schatz, G. C. The Optical Properties of Metal Nanoparticles: The Influence of Size, Shape, and Dielectric Environment. *J. Phys. Chem. B* **2003**, *107*, 668–677.
- (35) Xing, G. C.; Mathews, N.; Lim, S. S.; Yantara, N.; Liu, X. F.; Sabba, D.; Gratzel, M.; Mhaisalkar, S.; Sum, T. C. Low-Temperature Solution-Processed Wavelength-Tunable Perovskites for Lasing. *Nat. Mater.* **2014**, *13*, 476–480.
- (36) Ball, J. M.; et al. Optical Properties and Limiting Photocurrent of Thin-Film Perovskite Solar Cells. *Energy Environ. Sci.* **2015**, *8*, 602–609.
- (37) Chen, C. W.; Hsiao, S. Y.; Chen, C. Y.; Kang, H. W.; Huang, Z. Y.; Lin, H. W. Optical Properties of Organometal Halide Perovskite Thin Films and General Device Structure Design Rules for Perovskite Single and Tandem Solar Cells. *J. Mater. Chem. A* **2015**, *3*, 9152–9159.
- (38) Green, M. A.; Jiang, Y. J.; Soufiani, A. M.; Ho-Baillie, A. Optical Properties of Photovoltaic Organic-Inorganic Lead Halide Perovskites. *J. Phys. Chem. Lett.* **2015**, *6*, 4774–4785.
- (39) Ringe, E.; McMahon, J. M.; Sohn, K.; Cobley, C.; Xia, Y. N.; Huang, J. X.; Schatz, G. C.; Marks, L. D.; Van Duyne, R. P. Unraveling the Effects of Size, Composition, and Substrate on the Localized Surface Plasmon Resonance Frequencies of Gold and Silver Nanocubes: A Systematic Single-Particle Approach. *J. Phys. Chem. C* **2010**, *114*, 12511–12516.
- (40) Sum, T. C.; Mathews, N.; Xing, G. C.; Lim, S. S.; Chong, W. K.; Giovanni, D.; Dewi, H. A. Spectral Features and Charge Dynamics of Lead Halide Perovskites: Origins and Interpretations. *Acc. Chem. Res.* **2016**, *49*, 294–302.
- (41) Price, M. B.; Butkus, J.; Jellicoe, T. C.; Sadhanala, A.; Briane, A.; Halpert, J. E.; Broch, K.; Hodgkiss, J. M.; Friend, R. H.; Deschler, F. Hot-Carrier Cooling and Photoinduced Refractive Index Changes in Organic-Inorganic Lead Halide Perovskites. *Nat. Commun.* **2015**, *6*, No. 8420.
- (42) Del Fatti, N.; Voisin, C.; Achermann, M.; Tzortzakakis, S.; Christofilos, D.; Vallee, F. Nonequilibrium Electron Dynamics in Noble Metals. *Phys. Rev. B* **2000**, *61*, No. 16956.
- (43) Voisin, C.; Del Fatti, N.; Christofilos, D.; Vallee, F. Ultrafast Electron Dynamics and Optical Nonlinearities in Metal Nanoparticles. *J. Phys. Chem. B* **2001**, *105*, 2264–2280.
- (44) Furube, A.; Du, L.; Hara, K.; Katoh, R.; Tachiya, M. Ultrafast Plasmon-Induced Electron Transfer from Gold Nanodots into TiO<sub>2</sub> Nanoparticles. *J. Am. Chem. Soc.* **2007**, *129*, 14852–14853.
- (45) West, P. R.; Ishii, S.; Naik, G. V.; Emani, N. K.; Shalaev, V. M.; Boltasseva, A. Searching for Better Plasmonic Materials. *Laser Photonics Rev.* **2010**, *4*, 795–808.
- (46) Wu, K. F.; Rodriguez-Cordoba, W. E.; Yang, Y.; Lian, T. Q. Plasmon-Induced Hot Electron Transfer from the Au Tip to CdS Rod in CdS–Au Nanoheterostructures. *Nano Lett.* **2013**, *13*, 5255–5263.
- (47) Wu, K. F.; Zhu, H. M.; Liu, Z.; Rodriguez-Cordoba, W.; Lian, T. Q. Ultrafast Charge Separation and Long-Lived Charge Separated

State in Photocatalytic CdS-Pt Nanorod Heterostructures. *J. Am. Chem. Soc.* **2012**, *134*, 10337–10340.

(48) Chalabi, H.; Schoen, D.; Brongersma, M. L. Hot-Electron Photodetection with a Plasmonic Nanostripe Antenna. *Nano Lett.* **2014**, *14*, 1374–1380.

(49) Tanzid, M.; Ahmadvand, A.; Zhang, R. M.; Cerjan, B.; Sobhani, A.; Yazdi, S.; Nordlander, P.; Halas, N. J. Combining Plasmonic Hot Carrier Generation with Free Carrier Absorption for High-Performance Near-Infrared Silicon-Based Photodetection. *ACS Photonics* **2018**, *5*, 3472–3477.